Nano Research
2023, 16(6): 8321–8328

ISSN 1998-0124 CN 11-5974/O4
https://doi.org/10.1007/s12274-022-5018-7

Interfacial high-concentration electrolyte for stable lithium metal anode: Theory, design, and demonstration

Haotian Lu[1,2,3,4], Chunpeng Yang[2,3] (✉), Feifei Wang[1,2,3,4], Lu Wang[1,2,3,4], Jinghong Zhou[5], Wei Chen[1,4], and Quan-Hong Yang[1,2,3] (✉)

[1] *Joint School of National University of Singapore and Tianjin University, International Campus of Tianjin University, Fuzhou 350207, China*
[2] *Nanoyang Group, State Key Laboratory of Chemical Engineering, School of Chemical Engineering and Technology, and Collaborative Innovation Center of Chemical Science and Engineering (Tianjin), Tianjin University, Tianjin 300072, China*
[3] *Haihe Laboratory of Sustainable Chemical Transformations, Tianjin 300192, China*
[4] *Department of Chemistry, National University of Singapore, Singapore 117543, Singapore*
[5] *State-Key Laboratory of Chemical Engineering, East China University of Science of Technology, Shanghai 200237, China*

Received: 29 June 2022 / **Revised:** 20 August 2022 / **Accepted:** 5 September 2022

ABSTRACT

Lithium metal anodes hold great potential for high-energy-density secondary batteries. However, the uncontrollable lithium dendrite growth causes poor cycling efficiency and severe safety concerns, hindering lithium metal anode from practical application. Electrolyte components play important roles in suppressing lithium dendrite growth and improving the electrochemical performance of long-life lithium metal anode, and it is still challenging to effectively compromise the advantages of the conventional electrolyte (1 mol·L^{-1} salts) and high-concentration electrolyte (> 3 mol·L^{-1} salts) for the optimizing electrochemical performance. Herein, we propose and design an interfacial high-concentration electrolyte induced by the nitrogen- and oxygen-doped carbon nanosheets (NO-CNS) for stable Li metal anodes. The NO-CNS with abundant surface negative charges not only creates an interfacial high-concentration of lithium ions near the electrode surface to promote charge-transfer kinetics but also enables a high ionic conductivity in the bulk electrolyte to improve ionic mass-transfer. Benefitting from the interfacial high-concentration electrolyte, the NO-CNS@Ni foam host presents outstanding electrochemical cycling performances over 600 cycles at 1 mA·cm^{-2} and an improved cycling lifespan of 1,500 h for symmetric cells.

KEYWORDS

lithium metal anode, dendrite growth, interfacial high-concentration electrolyte, surface negative charge

1 Introduction

With over 30 years of development, lithium-ion (Li-ion) batteries have achieved a specific energy density of 260 Wh·kg^{-1} at the cell level and are approaching the theoretical limit of 300 Wh·kg^{-1} [1, 2]. Unfortunately, such an energy density cannot meet the increasing range demand (≥ 500 km with 500 Wh·kg^{-1}) for electric vehicles, which has raised great interest in developing advanced Li metal batteries with high energy density [3, 4]. The Li metal possesses a high theoretical specific capacity (3,860 mAh·g^{-1}) and the lowest electrochemical potential (–3.04 V versus the standard hydrogen electrode), and is considered one of the most promising anode materials [5–7]. However, the practical application of Li metal anode is still hindered by the uncontrollable growth of Li dendrite, which could cause low Coulombic efficiency (CE), poor cycling performance, and even potential safety hazards [8–10].

Many effective strategies have been proposed to suppress Li dendrite growth by regulating the kinetic and thermodynamic behaviors of Li deposition, coating functional interfacial layers to regulate Li-ion diffusion [11–15], engineering lithiophilic hosts to reduce Li nucleation overpotential [16–20], or constructing three-dimensional (3D) hosts to reduce local current density [21–25]. In principle, the electrodeposition process of Li-ions is normally controlled by the charge-transfer and the mass-transfer processes [26]. These transfer processes are highly dependent on the electric field, ionic concentration near the electrode surface [27, 28], and ionic conductivity in the bulk electrolyte [29, 30]. Typically, the ionic conductivity increases and then decreases as the ionic concentration increases, so the conventional electrolytes of 1 mol·L^{-1} (Fig. 1(a)) are considered to provide an optimal ionic conductivity, leading to the reduced overpotential induced by the mass-transfer process [31, 32]. The high-concentration electrolytes of ≥ 3 mol·L^{-1} (Fig. 1(b)) have poor ionic conductivity but attribute an enhanced kinetics of Li-ion reduction, leading to a reduced overpotential induced by charge-transfer process [33–35]. It is important to combine the advantages of conventional electrolytes and high-concentration electrolytes for reducing the electrodeposition overpotential and further mitigating Li dendrite growth.

An effective approach to combining the advantages of conventional electrolytes and high-concentration electrolytes is to form an interfacial high-concentration electrolyte (Fig. 1(c)). In the interfacial high-concentration electrolyte, there is a concentrated concentration of > 1 mol·L^{-1} Li-ions near the

Address correspondence to Chunpeng Yang, cpyang@tju.edu.cn; Quan-Hong Yang, qhyangcn@tju.edu.cn

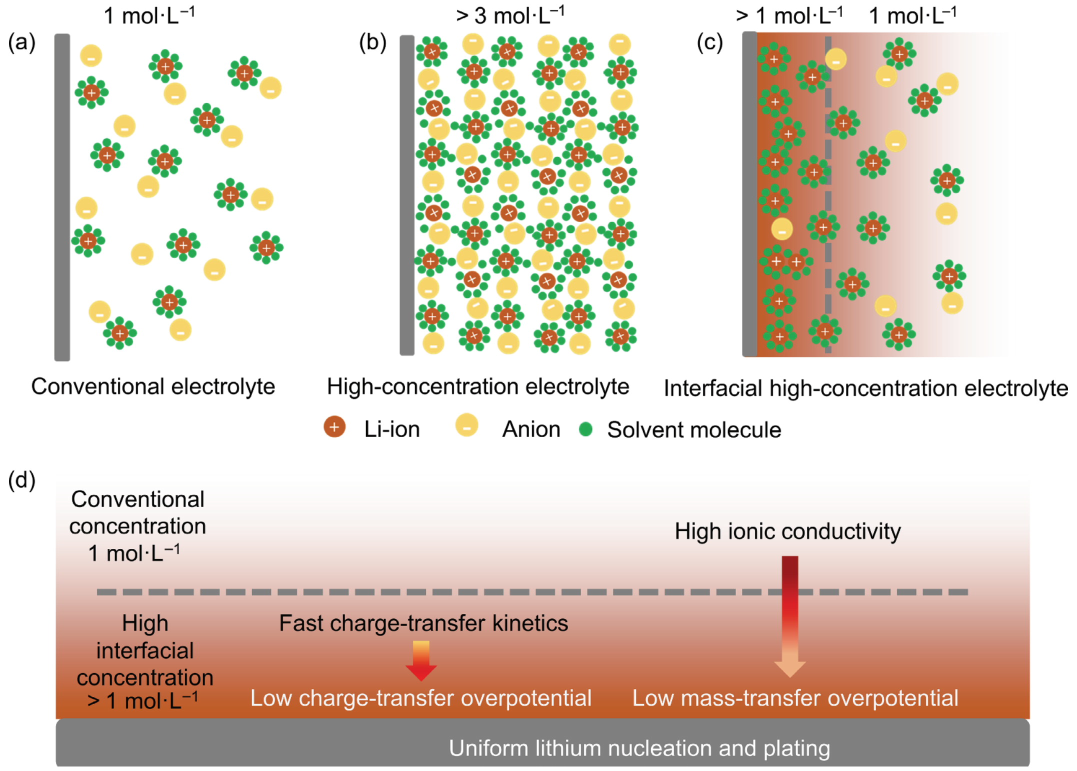

Figure 1 Schematic representatives of the ion distribution of (a) conventional electrolyte, (b) high-concentration electrolyte, and (c) interfacial high-concentration electrolyte. (d) Schematic illustration of the effect of the interfacial high-concentration electrolyte on lithium nucleation.

electrode surface, and a conventional concentration of 1 mol·L⁻¹ Li-ions in the bulk electrolyte. The regulation mechanism of interfacial high-concentration electrolyte on uniform Li deposition is schematically illustrated in Fig. 1(d), the reduction of Li-ions on the electrode has a relatively low charge-transfer overpotential induced by the high interfacial concentration of Li-ion. The mobility of Li-ions in the bulk electrolyte has a relatively low mass-transfer overpotential induced by the high ionic conductivity. These low potentials will result in the relatively uniform electrodeposition of Li-ion on the electrode. The classical simulations indicate that the electric field created by the charged surface can change the electrolyte structure and regulate ionic concentration near a charged surface [36–39]. Therefore, the interfacial high-concentration electrolyte can be realized by coating a surface charged material on the electrode, to develop for dendrite-free Li metal anode.

In this work, we design and showcase the interfacial high-concentration electrolyte behavior through a combination of simulation and experimental research. We first reveal the effect of negatively charged coating on inducing the interfacial high-concentration electrolyte through numerical simulations. As a proof-of-concept material, we coat nitrogen and oxygen co-doped carbon nanosheets (NO-CNS) with a massive surface negative charge on nickel foams (NO-CNS@Ni) to create the interfacial high-concertation electrolyte near the 3D host electrode. Benefiting from the *in-situ* formation of the interfacial high-concertation electrolyte, the NO-CNS@Ni foam as Li-host can effectively reduce the overpotential of Li nucleation, in good consistence with the theoretical prediction, and hence delivers excellent electrochemical performance in Li metal batteries.

2 Experimental and simulation

2.1 Preparation of NO-CNS and NO-CNS@Ni foam

Synthesis of NO-CNS: 3 g of melamine was placed in a crucible and then heated to 550 °C for 4 h at a heating rate of 5 °C·min⁻¹ in an air atmosphere to obtain graphitic carbon nitride (g-C_3N_4). 0.2 g of g-C_3N_4 and 0.6 g of K metal were mixed in an argon-filled glove box, and then were put into a Pyrex tube with a stop and a side vacuum connection. The tube was initially vacuumized with a vacuum pump to remove any evaporable phases and then heated to 190 °C for 4 h under the vacuum condition. After cooling down the tube to room temperature, the air was slowly introduced into the Pyrex tube. After the mixture was held for 30 min, 30 mL of ethanol and 30 mL of deionized (DI) water were successively added into the Pyrex tube. The mixture solution was sonicated for 2 h and then centrifuged at 5,000 rpm for 1 h to remove g-C_3N_4 sediment. The remaining K-ions in the solution were removed by a dialysis bag immersed in DI water for 1 week. Finally, 20 mL of NO-CNS aqueous solution was obtained by 50 °C heating and concentrating [40].

Fabrication of NO-C@Ni foam: Nickel foam was punched into a disk of 12 mm in diameter and pressed with a thickness of ~ 350 μm. Nickel foam was sequentially sonicated in ethanol and then dried in air to remove surface contaminants. Nickel foams were fully immersed in NO-CNS solution under ultrasonication for 10 min, and then dried at 60 °C to finally obtain NO-CNS@Ni foam electrodes, the loading of NO-CNS on Ni foam was about 0.02 mg·cm⁻².

2.2 Material characterization

The morphology and structure of material and electrode were characterized by scanning electron microscopy (SEM, Hitachi S4800), energy-dispersive X-ray spectroscopy (EDX), and transmission electron microscopy (TEM, JEM 3100F). X-ray diffraction (XRD) patterns were measured on a Bruker D-8 diffractometer (Cu Kα radiation, λ = 0.154 nm) at room temperature. The X-ray photoelectron spectra (XPS) measurements were carried out by using the Thermo Fisher Scientific K-Alpha+ (Al Kα radiation, $h\nu$ = 1,486.6 eV, UK) to analyze the valence state of the elements. Zeta potentials of NO-C solution were measured by Zetasizer Nano ZS (Malvern

Panalytical) at room temperature.

2.3 Electrochemical characterization

All CR2032-type coin cells were assembled in an Ar-filled glove box with oxygen and water content below 0.5 ppm. For coin half cells, the bare Ni foam and NO-CNS@Ni foam were employed as the working electrode. Lithium foil and polymer membrane (Celgard 2500) were employed as the reference/counter electrode and separator, respectively. The ether electrolyte was composed of 1 $mol{\cdot}L^{-1}$ bis(trifluoromethane sulfonyl)imide (LiTFSI) in 1,3-dioxolane:1,2-dimethoxyethane binary solvent (DOL:DME, 1:1 by volume) with 1 wt.% $LiNO_3$. For coin symmetrical cells, 6.0 $mAh{\cdot}cm^{-2}$ of Li was first predeposited on the Ni foam and NO-CNS@Ni foam in ether electrolyte to obtain Li@Ni foam and Li@NO-CNS@Ni foam. The Li@Ni foam or Li@NO-CNS@Ni foam was employed both as the electrode. The ether electrolyte and Celgard 2500 were employed as the electrolyte and separator, respectively. For coin full cells, Li@Ni foam or Li@NO-CNS@Ni foam with an areal capacity of 6 $mAh{\cdot}cm^{-2}$ was employed as the anode while commercial $LiFePO_4$ or $LiNi_{0.8}Co_{0.1}Mn_{0.1}O_2$ (NCM811) was employed as the cathode. Celgard 2500 was employed as the separator. The carbonate electrolyte was composed of 1 $mol{\cdot}L^{-1}$ lithium hexafluorophosphate ($LiPF_6$) in a mixed solution of ethylene carbonate (EC) and dimethyl carbonate (DMC) (EC:DMC, 1:1 by volume). The $LiFePO_4$ and NCM811 cathodes were made by casting slurries composed of $LiFePO_4$ (active material, 80 wt.%), super P (conductive carbon, 10 wt.%), and polyvinylidene difluoride (binder, 10 wt.%) in N-methyl-2pyrrolidone (NMP) solvent onto Al foils by a doctor blade and punching into a disk of 12 mm in diameter. The areal mass loading of $LiFePO_4$ active materials was controlled at around 5 $mg{\cdot}cm^{-2}$. The areal mass loading of NCM811 active materials was controlled at around 15 $mg{\cdot}cm^{-2}$.

For half-cell tests, a certain amount (e.g., 1.0 $mAh{\cdot}cm^{-2}$) of Li was deposited onto the working electrodes and then stripped to a cut-off voltage of 1.0 V at a certain current density (e.g., 1.0 $mA{\cdot}cm^{-2}$). The CE value was calculated based on the capacity ratio of stripped Li to deposited Li. The electrochemical impedance spectroscopy (EIS) was measured by Autolab Analyzer PGSTAT 128N (Metrohm, Switzerland). The frequency range was chosen between 100 kHz and 10 mHz. For symmetrical cell tests, a certain amount (e.g., 1.0 $mAh{\cdot}cm^{-2}$) of Li was deposited and then stripped at a certain current density (e.g., 1.0 $mA{\cdot}cm^{-2}$). For full-cell tests, the amount of pre-deposited Li for all anodes was 6 $mAh{\cdot}cm^{-2}$ accomplished by 6 h deposition at a current density of 1.0 $mA{\cdot}cm^{-2}$. The galvanostatic charge–discharge cycling tests were carried out in the Neware battery test system. The voltage range of 2.4–3.8 V was set for the full cell paired with the $LiFePO_4$ cathode. The voltage range of 2.8–4.2 V was set for the full cell paired with the NCM811 cathode.

2.4 Modeling and simulation details

The concentration distribution of Li-ion near electrode surfaces of different charge densities was captured based on the classical density functional theory (CDFT) [41]. Here, the real chemical potential of ions ($u_i = u_i^{ideal} + u_i^{ex}$) consists of the ideal chemical potential ($u_i^{ideal} = k_B T \ln c_i + z_i e \psi$, with c_i is the local ion concentration, z_i is the ion charge, k_B is the Boltzmann constant, T is the working temperature, e is the unit charge, and ψ is the local electrostatic potential) and the excess chemical potential ($u_i^{ex} = -k_B T \ln(1-\phi)$) that took into account the ionic volume effect (ϕ). The ionic volume effect was described by Bikerman's expression ($\phi = \sum_i^n a_i^3 c_i$, with a_i is the ionic diameter, and n is the total number of ionic species) [42]. Meanwhile, the electrostatic potential in the electrolyte solution satisfis the Poisson equation (Eq. (1)) [43], where ε_0 is the free space permittivity, ε_r is the relative permittivity of the electrolyte, N_A is the Avogadro constant

$$\nabla\cdot\varepsilon_0\varepsilon_r\nabla\psi = -\sum\nolimits_i^n z_i e N_A c_i \tag{1}$$

The temporal and spatial evolution of Li deposition morphology were captured by coupling the nonlinear phase-field model (PFM) (Eq. (2)), the Nernst–Plank equation (Eq. (3)) and the Poisson equation (Eq. (4)) [44]

$$\frac{\partial\xi}{\partial t} = -L_\sigma\left(g'(\xi) - \kappa\nabla^2\xi\right) - L_\eta h'(\xi)\left\{\begin{array}{c}\exp\left[\dfrac{(1-\alpha)F\eta}{RT}\right]\\ -c_{Li^+}\exp\left[\dfrac{-\alpha F\eta}{RT}\right]\end{array}\right\} \tag{2}$$

$$\frac{\partial c_{Li^+}}{\partial t} = \nabla\cdot\left(D_{Li^+}^{eff}\nabla c_{Li^+} + \frac{D_{Li^+}^{eff}c_{Li^+}}{RT}F\nabla\psi\right) - c_s\frac{\partial\xi}{\partial t} \tag{3}$$

$$\nabla\cdot\left(\sigma^{eff}\nabla\psi\right) = i_R \tag{4}$$

where ξ is the phase-field parameter ($\xi = 0$ for the electrolyte and $\xi = 1$ for the Li metal), $g(\xi)$ is the arbitrary double well function, κ is the surface energy anisotropy, L_σ is the interface mobility, L_η is the reaction-related constant, $h(\xi)$ is an interpolating function, α is the charge-transfer coefficient, η is the reaction overpotential, c_{Li^+} is the local Li-ion concentration, F is the Faraday's constant, $D_{Li^+}^{eff}$ is the effective diffusion coefficient of Li-ion, c_s is the site density of Li metal, σ^{eff} is the effective conductivity, and i_R is the current density. All models were solved by the finite element method on COMSOL Multiphysics 6.0. The parameters mentioned above are detailed in Table S1 in the Electronic Supplementary Material (ESM). The size and structure of the simulated models are detailed in Figs. S1 and S2 in the ESM.

3 Results and discussion

3.1 The *in-situ* formation of the interfacial high-concentration electrolyte

Figure 2(a) illustrates the *in-situ* formation mechanism of the interfacial high-concentration electrolyte. When the current collector has a surface with negative charges, the positively charged Li-ion concentration near the charged surface increases to maintain overall charge conservation, resulting in the interfacial high-concentration Li-ion electrolyte [37, 45]. Motivated by the above mechanism, we coated the current collector with a surface negatively charged material which then *in-situ* forms an interfacial high-concentration electrolyte in batteries. The NO-CNS was synthesized through the exfoliation and disintegration of the bulk g-C_3N_4. The strong reaction between K-treated g-C_3N_4 and ethanol/water splits the bulk g-C_3N_4 into the mono-layer or few-layer porous nanosheets (Fig. 2(b) and Fig. S5(a) in the ESM). As shown in Fig. 2(c), the obtained NO-CNS presents a negative zeta-potential of −18.28 mV, indicating that the NO-CNS is an appropriate proof-of-concept material with a lot of negative charges. According to the XRD patterns (Fig. 2(d)), the NO-CNS shows no obvious (100) peak corresponding to the in-plane packing of the bulk g-C_3N_4, which confirms the severe destruction of heptazine rings [46]. XPS analysis of NO-CNS (Fig. 2(e)) shows the amount of C atoms (86.49 at.%) significantly is higher than the total amounts of N atoms (9.83 at.%) and O atoms (2.95 at.%), indicating the partial removal of N atoms and the introduction of O atoms in the heptazine rings. Meanwhile, the C 1s XPS spectrum of NO-CNS (Fig. 2(f)) shows that the relative intensity of the N=C–N peak is much lower than that of C–O and C–C

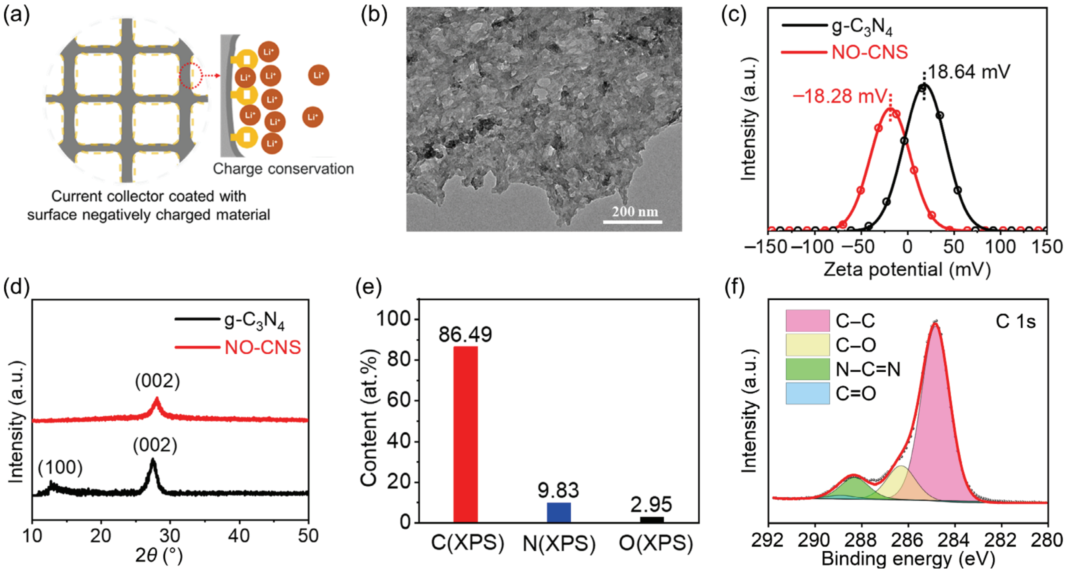

Figure 2 (a) Schematic illustration of the formation mechanism of the interfacial high-concentration electrolyte. (b) TEM image of NO-CNS. (c) Zeta potentials of NO-CNS and g-C_3N_4 solutions. (d) XRD patterns of NO-CNS and bulk g-C_3N_4. (e) Surface atomic content of different elements on the NO-CNS obtained by XPS measurement. (f) High-resolution C 1s XPS spectrum of NO-CNS.

peaks, further indicating the severe destruction of the heptazine ring and the formation of edged C [47, 48]. Therefore, the surface negative charges of NO-CNS mainly come from the unpaired electrons the edged C induced by the partial removal of N atoms in the heptazine rings. In order to eliminate the influence of the limiting current density on the electrodeposition of Li-ion, the 3D Ni foam was chosen as the substrate to be modified, due to its large surface area to reduce local current density [21–24].

The NO-CNS was coated on the Ni foams through the impregnation and drying processes. The SEM images with the EDX mappings (Fig. 3(a)) illustrate that C, N, and O elements are evenly distributed in the NO-CNS@Ni foam framework, demonstrating that the NO-CNS with a surface negative charge has been uniformly coated on the surface of the Ni foam. To evaluate the effects of the surface negative charge of NO-CNS@Ni foam on the electrolyte structure, the ionic distribution was visualized based on the CDFT simulation (Figs. S1 and S3 in the ESM). As shown in Fig. 3(b), there is an obvious interfacial high concertation of Li-ions near the negatively charged electrode surface. When the density of surface negative charge (expressed by electrostatic potential [49, 50]) is increased to −20 mV, the concentration of Li-ions accumulated at the electrode interface is even as high as 2.2 mol·L^{-1}. The nucleation overpotentials were further obtained based on the Nernst equation as shown in Fig. S4 in the ESM. With the interfacial concentration of Li-ion increasing, the nucleation overpotential distinctly decreases, which provides a convenient condition for the uniform nucleation of Li metal [27]. Subsequently, as Li metal nucleates more uniformly, the growth of Li dendrite is slowed down (Figs. 3(c)–3(e)), which further favors uniform Li plating. In view of the above results, for the interfacial high-concentration electrolyte induced by the surface negative charge of NO-CNS@Ni foam, the nucleation overpotential will be much lower than that of the conventional electrolyte, thus allowing uniform electrodeposition of Li-ions.

3.2 Performance of Li electrodeposition in the interfacial high-concentration electrolyte

To further confirm the effectiveness of the interfacial high-concentration electrolyte induced by the surface negatively charged NO-CNS@Ni foam in practical systems, we studied the electrochemical performance of half cells using the Li host (NO-CNS@Ni foam and Ni foam) as the working electrode and Li foil as the counter/reference electrode. The Nyquist plots in Fig. 4(a) compare the impedance of the half cells with bare Ni foam and NO-CNS@Ni foam. The half-cell with the coating NO-CNS layer shows a much smaller charge-transfer resistance value (13.70 Ω) than that without the coating layer (20.26 Ω). However, the activation energy of charge transfer for the NO-CNS@Ni foam electrode (60.55 kJ·mol^{-1}) is slightly higher than that of the Ni foam electrode (58.02 kJ·mol^{-1}, Fig. S7 in the ESM). The above results indicate the reduced charge-transfer resistance of NO-CNS@Ni foam is mainly attributed to the formation of an interfacial high-concentration electrolyte rather than the change of reaction activation energy, promoting the charge-transfer kinetics of plating Li on the electrode surface. The nucleation overpotential, which is the potential difference between the lowest value and stabilized one in the electrodeposition process, is an important parameter to evaluate the Li nucleation process. As shown in Fig. 4(b), the nucleation overpotential of Li plating on NO-CNS@Ni foam is only 53.0 mV at the current density of 1.0 mA·cm^{-2}, much smaller than that of Li plating Ni foam (143.9 mV), further demonstrating less kinetic resistance in nucleation and uniform Li nucleation for the NO-CNS modified Ni foam electrode compared with the pristine Ni foam electrode. Notably, the nucleation overpotential of Ni foam increases significantly with the current density (49 mV at 0.2 mA·cm^{-2}, 65.4 mV at 0.5 mA·cm^{-2}, 143.9 mV at 1.0 mA·cm^{-2}, Fig. S8 in the ESM). In contrast, the nucleation overpotential of NO-CNS modified Ni foam is almost not affected by the current density (47.7 mV at 0.2 mA·cm^{-2}, 52.2 mV at 0.5 mA·cm^{-2}, 53 mV at 1.0 mA·cm^{-2}, Fig. S8 in the ESM). This indicates that the high concentration of Li-ions at the NO-CNS@Ni interface exempts the Li nucleation from the mass-transfer limitations even at high current density, beneficial to uniform Li nucleation and the subsequent Li plating.

The uniform Li nucleation benefiting from the interfacial high-concentration electrolyte effectively ensures the controlled electrodeposition of the Li-ions on the host. The morphologies of Li plating on the NO-CNS@Ni foam and Ni foam electrodes are significantly different, as compared in Figs. 4(c) and 4(d). After plating a capacity of 1.0 mAh·cm^{-2}, the plated Li is uniformly distributed on the surface of NO-C@Ni foam. In contrast, the Li plated in Ni foam agglomerated on the surface. After further increasing the capacity of plating Li, there are agglomerated morphology and even Li dendrites on the surface of pristine Ni

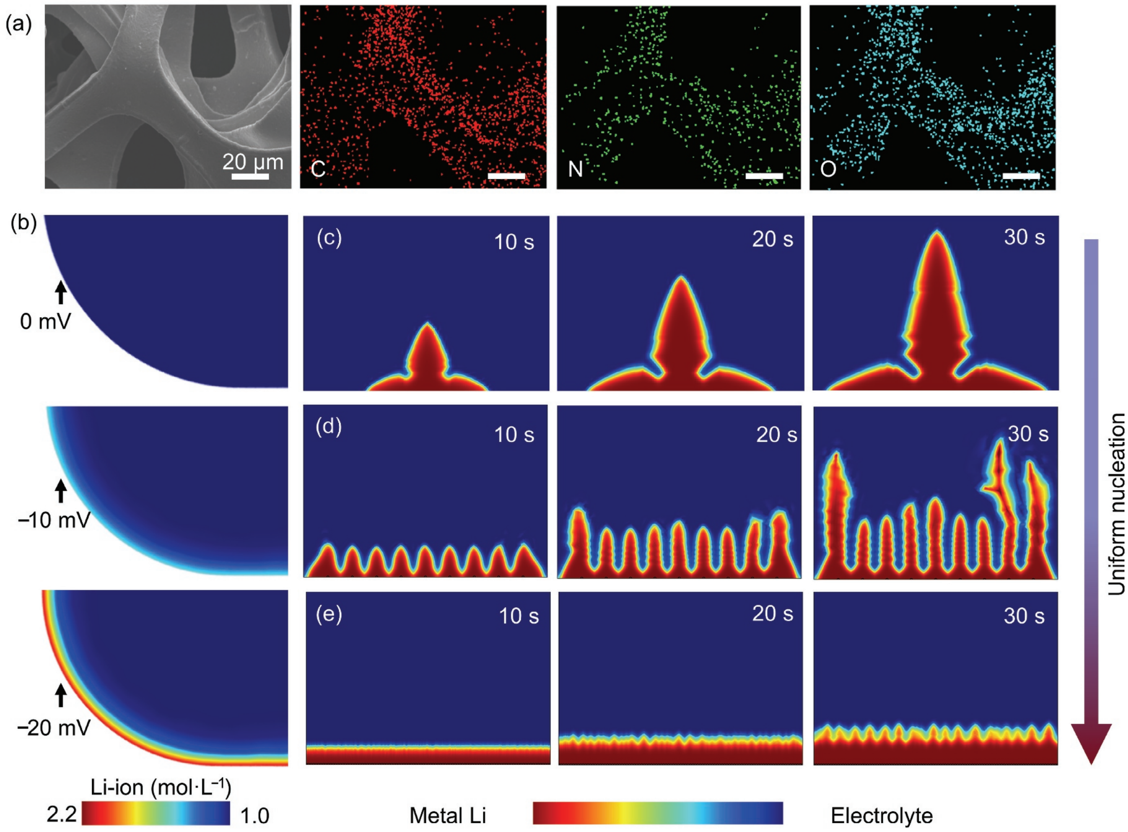

Figure 3 (a) SEM image of NO-CNS@Ni foam and EDS mapping images of C, N, and O of NO-CNS@Ni foam. (b) Simulation results of the Li-ion concentration distribution near the current collector with the different amounts of surface negative charge (expressed by the electrostatic potential). (c)–(e) The simulated dendritic morphology evolution under different uniformities of initial nucleation.

foam. In contrast, the surface of the Li@NO-CNS@Ni foam electrode remains relatively flat, which is attributed to uniform nucleation during initial Li plating. The effective dendrite suppression arising from the interfacial high-concentration electrolyte ensures the cycling stability and long life of the Li metal anodes. As shown in Fig. 4(e), the NO-CNS@Ni foam electrode achieves more than 600 cycles at a current density of 1.0 mA·cm^{-2} with a capacity of 1.0 mAh·cm^{-2}, much better than the Ni foam electrode with a rapid short circuit within 250 cycles. Even at a high current density of 2.0 mA·cm^{-2} with a high capacity of 2.0 mAh·cm^{-2}, NO-CNS@Ni foam electrode still stably works over 150 cycles, superior to Ni foam electrode with a fast failure after 80 cycles (Fig. S9 in the ESM). Furthermore, when the pre-deposited electrodes with a Li-capacity of 6.0 mAh·cm^{-2} are assembled into the symmetric cell, the Li@NO-CNS@Ni foam symmetric cell displays stable and low voltage hysteresis for more than 1,500 h at a current density of 1.0 mA·cm^{-2} with a capacity of 1.0 mAh·cm^{-2}, but the voltage hysteresis overshoots for the Li@Ni foam symmetric cell after 600 h (Fig. 4(f)). Thus, the interfacial high-concentration electrolyte induced by negatively charged surface improves the electrochemical kinetics of Li deposition and suppressed Li dendrite growth, and then improves the cycling stability of Li metal anode.

The superior cycling stability of Li@NO-CNS@Ni arising from the interfacial high-concentration electrolyte improves the full battery performances of the Li metal batteries. The Li@NO-CNS@Ni||$LiFePO_4$ battery exhibits a high capacity of up to 137.6 mAh·g^{-1} (based on cathode mass) at the current density of 0.2 C (1 C = 170 mA·g^{-1}). When increasing the current rate to 0.5 C, a capacity of 133.3 mAh·g^{-1} can still be obtained, indicating a high-rate capability (Fig. 5(a)). The Li@NO-CNS@Ni||$LiFePO_4$ battery exhibits high discharge capacities of 137.6 mAh·g^{-1} at 0.2 C, 133.3 mAh·g^{-1} at 0.5 C, 123.9 mAh·g^{-1} at 1.0 C, 106.6 mAh·g^{-1} at 2.0 C, 59.5 mAh·g^{-1} at 5.0 C and then back to 120.7 mAh·g^{-1} at 1.0 C, all higher than those of Li@Ni||$LiFePO_4$ battery (Fig. 5(b)), confirming the high rate capability of NO-CNS@Ni foam electrode to pure Ni foam electrode. We also compared the cycling performances of Li@Ni||$LiFePO_4$ and Li@NO-CNS@Ni||$LiFePO_4$ batteries at 1.0 C (Fig. 5(c)). The capacity retention of the Li@Ni||$LiFePO_4$ battery rapidly fades to less than 10% after 40 cycles. In contrast, the Li@NO-CNS@Ni||$LiFePO_4$ battery stably runs over 60 cycles with a capacity retention of ~ 90%. In addition, we further evaluated the rate capabilities of Li@Ni||$LiFePO_4$ and Li@NO-CNS@Ni||$LiFePO_4$ batteries. Even when the Li@NO-CNS@Ni electrode is paired with the NCM811 cathode with a high areal capacity of ~ 4.1 mAh·cm^{-2}, the battery can stably run over 80 cycles with a capacity retention of ~ 80% at a 1.0 C (1 C = 200 mA·g^{-1}, Fig. 5(d)). Thus, the interfacial high-concentration electrolyte induced by negatively charged NO-CNS coating is beneficial for the practical application of the Li metal anode.

4 Conclusions

In summary, we show that the interfacial high-concentration electrolyte, induced by the surface negatively charged coating, can effectively reduce the electrodeposition overpotential of plating Li-ions on a host to restrain the Li dendrite growth. NO-CNS with surface negative charges, as a proof-of-concept material, was coated on Ni foam to get the NO-CNS@Ni foam electrode. According to the charge conservation principle, the positively charged Li-ions are concentered near the NO-CNS@Ni foam electrode surface, which promotes the charge transfer kinetics of plating Li-ions on the NO-CNS@Ni foam electrode. As result, both half-cell and full-cell tests based on the NO-CNS@Ni foam electrode show the low nucleation overpotential, the smooth Li morphology, the excellent cycling stability, and the long life for Li

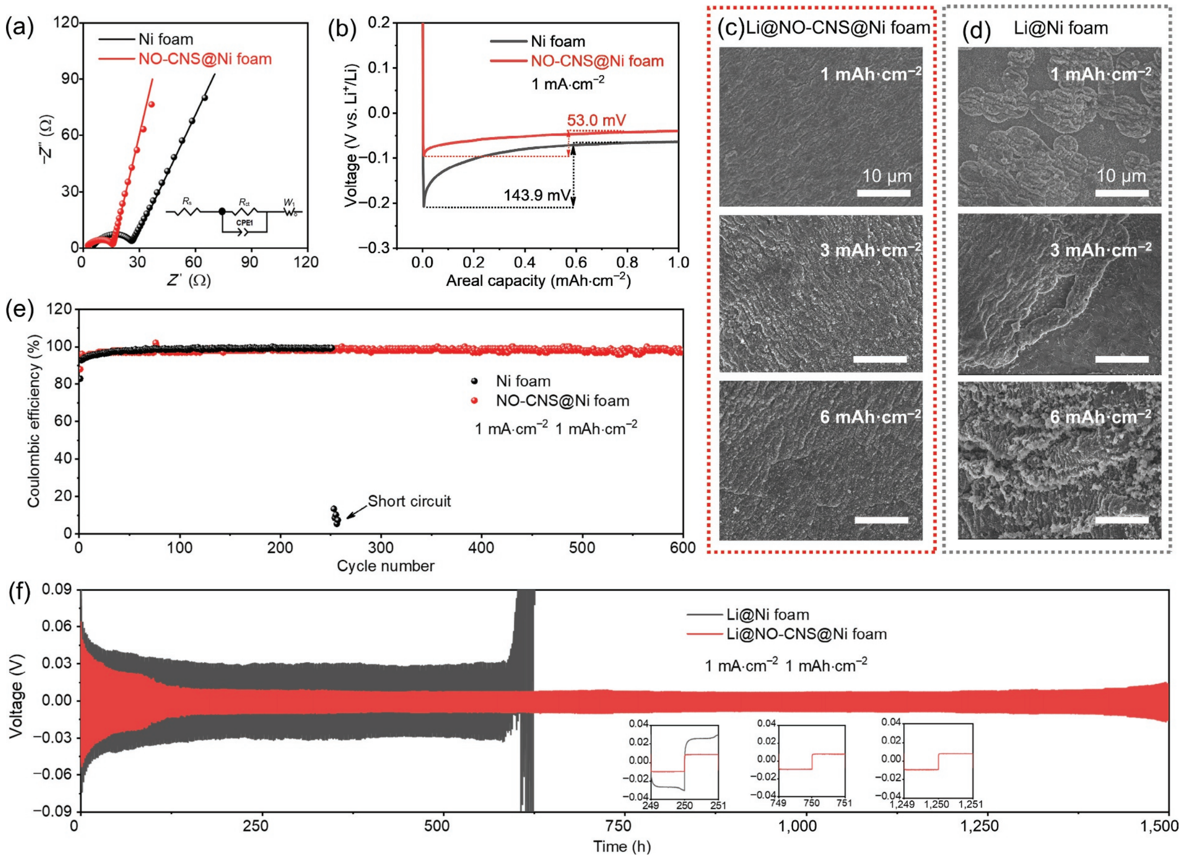

Figure 4 (a) The Nyquist plots of half cells assembled with Ni foam||Li foil and NO-CNS@Ni foam||Li foil. (b) The voltage–capacity profiles of Li plating on the Ni foam and NO-CNS@Ni foam electrodes at 1.0 mA·cm^{-2}. SEM images of Li deposition morphologies in (c) Ni foam electrode and (d) NO-CNS@Ni foam electrode. (e) Coulombic efficiency for the Li plating and stripping on Ni foam and NO-CNS@Ni foam electrodes at a current density of 1.0 mA·cm^{-2} with a capacity of 1 mAh·cm^{-2}. (f) Galvanostatic discharge/charge voltage profiles of the Li@Ni foam electrode and Li@NO-CNS@Ni foam electrode in symmetric cells at a current density of 1.0 mA·cm^{-2} with a fixed capacity of 1 mAh·cm^{-2}.

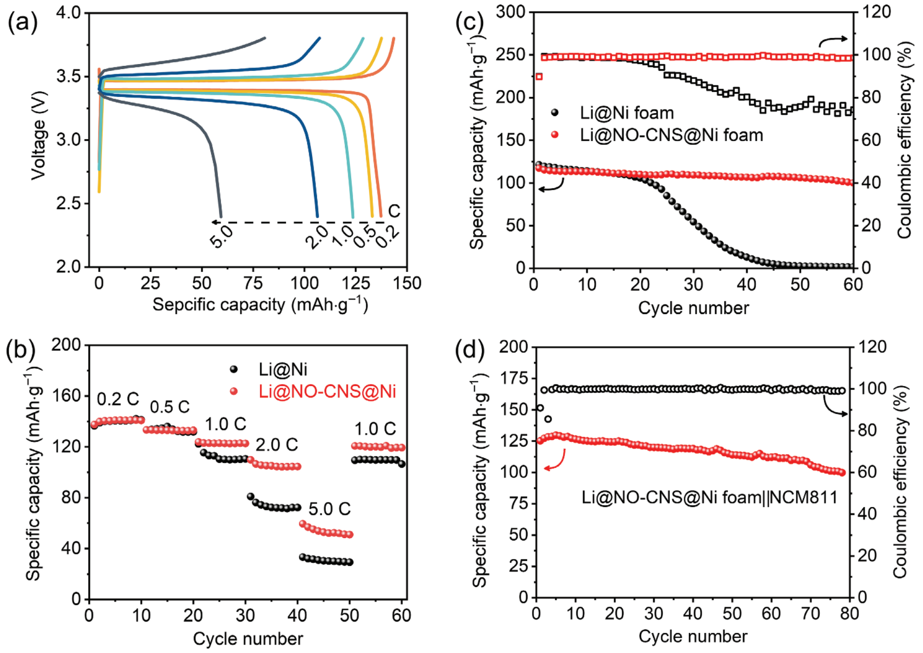

Figure 5 (a) Voltage–capacity profiles of Li@NO-CNS@Ni foam||LiFePO$_4$ at different rates. (b) Rate performance and (c) cycling performance of Li@Ni foam||LiFePO$_4$ in carbonate electrolyte. (d) Cycling performance of Li@NO-CNS@Ni foam||NCM811 in carbonate electrolyte.

plating/stripping, much better than counterparts based on pure Ni foam electrode. This provides a simple principle for suppressing the lithium dendrites by simultaneously taking into account the advantages of conventional electrolyte and high-concentration electrolyte for stable Li metal anode, which may be applied to other substrates for the practical metal batteries.

Acknowledgements

This research was supported by the National Key Research and Development Program of China (No. 2021YFF0500600), the Haihe Laboratory of Sustainable Chemical Transformations, and the Fundamental Research Funds for the Central Universities. We appreciate Neware Technology Co., Ltd for their battery test systems in the TJU Nanoyang-Neware Joint Laboratory for Energy Innovation.

Electronic Supplementary Material: Supplementary material (simulation parameters, Li-ion and anion distribution, TEM and XPS of NO-CNS, and other electrochemical results) is available in the online version of this article at https://doi.org/10.1007/s12274-022-5018-7.

References

[1] Armand, M.; Tarascon, J. M. Building better batteries. *Nature* **2008**, *451*, 652–657.

[2] Van Noorden, R. The rechargeable revolution: A better battery. *Nature* **2014**, *507*, 26–28.

[3] Liu, J.; Bao, Z. N.; Cui, Y.; Dufek, E. J.; Goodenough, J. B.; Khalifah, P.; Li, Q. Y.; Liaw, B. Y.; Liu, P.; Manthiram, A. et al. Pathways for practical high-energy long-cycling lithium metal batteries. *Nat. Energy* **2019**, *4*, 180–186.

[4] Li, M.; Lu, J.; Chen, Z. W.; Amine, K. 30 years of lithium-ion batteries. *Adv. Mater.* **2018**, *30*, 1800561.

[5] Xu, W.; Wang, J. L.; Ding, F.; Chen, X. L.; Nasybulin, E.; Zhang, Y. H.; Zhang, J. G. Lithium metal anodes for rechargeable batteries. *Energy Environ. Sci.* **2014**, *7*, 513–537.

[6] Bruce, P. G.; Freunberger, S. A.; Hardwick, L. J.; Tarascon, J. M. Li-O$_2$ and Li-S batteries with high energy storage. *Nat. Mater.* **2012**, *11*, 19–29.

[7] Zeng, X. Q.; Li, M.; Abd El-Hady, D.; Alshitari, W.; Al-Bogami, A. S.; Lu, J.; Amine, K. Commercialization of lithium battery technologies for electric vehicles. *Adv. Energy Mater.* **2019**, *9*, 1900161.

[8] Zhang, Y. F.; Wu, S. C.; Yang, Q. H. Revisiting lithium metal anodes from a dynamic and realistic perspective. *EnergyChem* **2021**, *3*, 100063.

[9] Zhang, X.; Yang, Y. A.; Zhou, Z. Towards practical lithium-metal anodes. *Chem. Soc. Rev.* **2020**, *49*, 3040–3071.

[10] Ren, W. C.; Zheng, Y. N.; Cui, Z. H.; Tao, Y. S.; Li, B. X.; Wang, W. T. Recent progress of functional separators in dendrite inhibition for lithium metal batteries. *Energy Storage Mater.* **2021**, *35*, 157–168.

[11] Nan, Y.; Li, S. M.; Han, C.; Yan, H. B.; Ma, Y. X.; Liu, J. H.; Yang, S. B.; Li, B. Interlamellar lithium-ion conductor reformed interface for high performance lithium metal anode. *Adv. Funct. Mater.* **2021**, *31*, 2102336.

[12] Huang, Z. J.; Choudhury, S.; Gong, H. X.; Cui, Y.; Bao, Z. N. A cation-tethered flowable polymeric interface for enabling stable deposition of metallic lithium. *J. Am. Chem. Soc.* **2020**, *142*, 21393–21403.

[13] Jang, E. K.; Ahn, J.; Yoon, S.; Cho, K. Y. High dielectric, robust composite protective layer for dendrite-free and LiPF$_6$ degradation-free lithium metal anode. *Adv. Funct. Mater.* **2019**, *29*, 1905078.

[14] He, Y. T.; Zhang, Y. H.; Sari, H. M. K.; Wang, Z. H.; Lü, Z.; Huang, X. Q.; Liu, Z. G.; Zhang, J. J.; Li, X. F. New insight into Li metal protection: Regulating the Li-ion flux via dielectric polarization. *Nano Energy* **2021**, *89*, 106334.

[15] Xu, Q.; Li, Y. N.; Wu, C. H.; Sun, X. T.; Li, Q.; Zhang, H. B.; Yu, L.; Pan, Y. Y.; Wang, Y. J.; Guo, S. W. et al. Kinetically accelerated and high-mass loaded lithium storage enabled by atomic iron embedded carbon nanofibers. *Nano Res.* **2022**, *15*, 6176–6183.

[16] Yan, K.; Lu, Z. D.; Lee, H. W.; Xiong, F.; Hsu, P. C.; Li, Y. Z.; Zhao, J.; Chu, S.; Cui, Y. Selective deposition and stable encapsulation of lithium through heterogeneous seeded growth. *Nat. Energy* **2016**, *1*, 16010.

[17] Zhang, C.; Lv, W.; Zhou, G. M.; Huang, Z. J.; Zhang, Y. B.; Lyu, R.; Wu, H. L.; Yun, Q. B.; Kang, F. Y.; Yang, Q. H. Vertically aligned lithiophilic CuO nanosheets on a Cu collector to stabilize lithium deposition for lithium metal batteries. *Adv. Energy Mater.* **2018**, *8*, 1703404.

[18] Yang, C. P.; Yao, Y. G.; He, S. M.; Xie, H.; Hitz, E.; Hu, L. B. Ultrafine silver nanoparticles for seeded lithium deposition toward stable lithium metal anode. *Adv. Mater.* **2017**, *29*, 1702714.

[19] Li, S. Y.; Wang, W. P.; Xin, S.; Zhang, J.; Guo, Y. G. A facile strategy to reconcile 3D anodes and ceramic electrolytes for stable solid-state Li metal batteries. *Energy Storage Mater.* **2020**, *32*, 458–464.

[20] Wen, Z. P.; Peng, Y. Y.; Cong, J. L.; Hua, H. M.; Lin, Y. X.; Xiong, J.; Zeng, J.; Zhao, J. B. A stable artificial protective layer for high capacity dendrite-free lithium metal anode. *Nano Res.* **2019**, *12*, 2535–2542.

[21] Yang, C. P.; Yin, Y. X.; Zhang, S. F.; Li, N. W.; Guo, Y. G. Accommodating lithium into 3D current collectors with a submicron skeleton towards long-life lithium metal anodes. *Nat. Commun.* **2015**, *6*, 8058.

[22] Xu, Z. X.; Xu, L. Y.; Xu, Z. X.; Deng, Z. P.; Wang, X. L. N, O-codoped carbon nanosheet array enabling stable lithium metal anode. *Adv. Funct. Mater.* **2021**, *31*, 2102354.

[23] Yang, T. Y.; Li, L.; Wu, F.; Chen, R. J. A soft lithiophilic graphene aerogel for stable lithium metal anode. *Adv. Funct. Mater.* **2020**, *30*, 2002013.

[24] Feng, X. Y.; Wu, H. H.; Gao, B.; Świętosławski, M.; He, X.; Zhang, Q. B. Lithiophilic N-doped carbon bowls induced Li deposition in layered graphene film for advanced lithium metal batteries. *Nano Res.* **2022**, *15*, 352–360.

[25] Zhang, Y.; Liu, B. Y.; Hitz, E.; Luo, W.; Yao, Y. G.; Li, Y. J.; Dai, J. Q.; Chen, C. J.; Wang, Y. B.; Yang, C. P. et al. A carbon-based 3D current collector with surface protection for Li metal anode. *Nano Res.* **2017**, *10*, 1356–1365.

[26] Chen, X. R.; Yao, Y. X.; Yan, C.; Zhang, R.; Cheng, X. B.; Zhang, Q. A diffusion-reaction competition mechanism to tailor lithium deposition for lithium-metal batteries. *Angew. Chem., Int. Ed.* **2020**, *59*, 7743–7747.

[27] Xu, X. Y.; Liu, Y. Y.; Hwang, J. Y.; Kapitanova, O. O.; Song, Z. X.; Sun, Y. K.; Matic, A.; Xiong, S. Z. Role of Li-ion depletion on electrode surface: Underlying mechanism for electrodeposition behavior of lithium metal anode. *Adv. Energy Mater.* **2020**, *10*, 2002390.

[28] Lee, Y.; Ma, B. Y.; Bai, P. Concentration polarization and metal dendrite initiation in isolated electrolyte microchannels. *Energy Environ. Sci.* **2020**, *13*, 3504–3513.

[29] Cheng, X. B.; Zhang, R.; Zhao, C. Z.; Zhang, Q. Toward safe lithium metal anode in rechargeable batteries: A review. *Chem. Rev.* **2017**, *117*, 10403–10473.

[30] Yang, Y. Y. C.; Davies, D. M.; Yin, Y. J.; Borodin, O.; Lee, J. Z.; Fang, C. C.; Olguin, M.; Zhang, Y. H.; Sablina, E. S.; Wang, X. F. et al. High-efficiency lithium-metal anode enabled by liquefied gas electrolytes. *Joule* **2019**, *3*, 1986–2000.

[31] Yamada, Y.; Furukawa, K.; Sodeyama, K.; Kikuchi, K.; Yaegashi, M.; Tateyama, Y.; Yamada, A. Unusual stability of acetonitrile-based superconcentrated electrolytes for fast-charging lithium-ion batteries. *J. Am. Chem. Soc.* **2014**, *136*, 5039–5046.

[32] Kremer, L. S.; Danner, T.; Hein, S.; Hoffmann, A.; Prifling, B.; Schmidt, V.; Latz, A.; Wohlfahrt-Mehrens, M. Influence of the electrolyte salt concentration on the rate capability of ultra-thick NCM 622 electrodes. *Batteries Supercaps* **2020**, *3*, 1172–1182.

[33] Jiang, G. X.; Li, F.; Wang, H. P.; Wu, M. G.; Qi, S. H.; Liu, X. H.; Yang, S. C.; Ma, J. M. Perspective on high-concentration electrolytes for lithium metal batteries. *Small Struct.* **2021**, *2*, 2000122.

[34] Xu, Y. L.; Dong, K.; Jie, Y. L.; Adelhelm, P.; Chen, Y. W.; Xu, L.; Yu, P. P.; Kim, J.; Kochovski, Z.; Yu, Z. L. et al. Promoting mechanistic understanding of lithium deposition and solid-electrolyte interphase (SEI) formation using advanced characterization and simulation methods: Recent progress, limitations, and future perspectives. *Adv. Energy Mater.* **2022**, *12*, 2200398.

[35] Sodeyama, K.; Yamada, Y.; Aikawa, K.; Yamada, A.; Tateyama, Y. Sacrificial anion reduction mechanism for electrochemical stability improvement in highly concentrated Li-salt electrolyte. *J. Phys. Chem. C* **2014**, *118*, 14091–14097.

[36] Hamad, I. A.; Novotny, M. A.; Wipf, D. O.; Rikvold, P. A. A new battery-charging method suggested by molecular dynamics

simulations. *Phys. Chem. Chem. Phys.* **2010**, *12*, 2740–2743.

[37] Jorn, R.; Kumar, R.; Abraham, D. P.; Voth, G. A. Atomistic modeling of the electrode–electrolyte interface in Li-ion energy storage systems: Electrolyte structuring. *J. Phys. Chem. C* **2013**, *117*, 3747–3761.

[38] Dewan, S.; Carnevale, V.; Bankura, A.; Eftekhari-Bafrooei, A.; Fiorin, G.; Klein, M. L.; Borguet, E. Structure of water at charged interfaces: A molecular dynamics study. *Langmuir* **2014**, *30*, 8056–8065.

[39] Li, Y. S.; Qi, Y. Energy landscape of the charge transfer reaction at the complex Li/SEI/electrolyte interface. *Energy Environ. Sci.* **2019**, *12*, 1286–1295.

[40] Lin, L. X.; Xu, Y. X.; Zhang, S. W.; Ross, I. M.; Ong, A. C. M.; Allwood, D. A. Fabrication and luminescence of monolayered boron nitride quantum dots. *Small* **2014**, *10*, 60–65.

[41] Biesheuvel, P. M.; Van Soestbergen, M. Counterion volume effects in mixed electrical double layers. *J. Colloid Interface Sci.* **2007**, *316*, 490–499.

[42] Bikerman, J. J. Structure and capacity of electrical double layer. *London Edinburgh Dublin Philos. Mag. J. Sci.* **1942**, *33*, 384–397.

[43] Varghese, J.; Wang, H. N.; Pilon, L. Simulating electric double layer capacitance of mesoporous electrodes with cylindrical pores. *J. Electrochem. Soc.* **2011**, *158*, A1106.

[44] Chen, L.; Zhang, H. W.; Liang, L. Y.; Liu, Z.; Qi, Y.; Lu, P.; Chen, J.; Chen, L. Q. Modulation of dendritic patterns during electrodeposition: A nonlinear phase-field model. *J. Power Sources* **2015**, *300*, 376–385.

[45] Yang, H. C.; Yang, J. Y.; Bo, Z.; Chen, X.; Shuai, X. R.; Kong, J.; Yan, J. H.; Cen, K. F. Kinetic-dominated charging mechanism within representative aqueous electrolyte-based electric double-layer capacitors. *J. Phys. Chem. Lett.* **2017**, *8*, 3703–3710.

[46] Lu, Z. Y.; Liang, Q. H.; Wang, B.; Tao, Y.; Zhao, Y. F.; Lv, W.; Liu, D. H.; Zhang, C.; Weng, Z.; Liang, J. C. et al. Graphitic carbon nitride induced micro-electric field for dendrite-free lithium metal anodes. *Adv. Energy Mater.* **2019**, *9*, 1803186.

[47] Gao, H. L.; Yan, S. C.; Wang, J. J.; Huang, Y. A.; Wang, P.; Li, Z. S.; Zou, Z. G. Towards efficient solar hydrogen production by intercalated carbon nitride photocatalyst. *Phys. Chem. Chem. Phys.* **2013**, *15*, 18077–18084.

[48] Tong, Z. M.; Huang, L.; Liu, H. P.; Lei, W.; Zhang, H. J.; Zhang, S. W.; Jia, Q. L. Defective graphitic carbon nitride modified separators with efficient polysulfide traps and catalytic sites for fast and reliable sulfur electrochemistry. *Adv. Funct. Mater.* **2021**, *31*, 2010455.

[49] Merlet, C.; Péan, C.; Rotenberg, B.; Madden, P. A.; Simon, P.; Salanne, M. Simulating supercapacitors: Can we model electrodes as constant charge surfaces? *J. Phys. Chem. Lett.* **2013**, *4*, 264–268.

[50] Wang, Z. X.; Yang, Y.; Olmsted, D. L.; Asta, M.; Laird, B. B. Evaluation of the constant potential method in simulating electric double-layer capacitors. *J. Chem. Phys.* **2014**, *141*, 184102.